J Physiol 587.22 (2009) pp 5377–5391

The Journal of Physiology

Loose coupling between calcium channels and sites of exocytosis in chromaffin cells

Minnie M. Wu, Artur Llobet and Leon Lagnado

MRC Laboratory of Molecular Biology, Hills Road, Cambridge CB2 2QH, UK

Calcium microdomains generated by tight clusters of calcium channels regulate fusion of small vesicles at the synaptic terminal and have also been suggested to trigger exocytosis of large dense-core vesicles from neuroendocrine cells. To test this idea, we have compared sites of exocytosis and the spatial distribution of calcium channels in chromaffin cells. Fusion of individual vesicles was visualized using interference reflection microscopy and the submembranous calcium signal was assessed using total internal reflection fluorescence microscopy. Depolarization triggered a burst of exocytosis from up to seven sites in a membrane area of 11 μm^2, but these sites did not colocalize with calcium microdomains. Instead, calcium influx occurred in large patches (averaging 34 μm^2) containing a mixture of P/Q- and N-type channels. About 20% of fusion events occurred outside calcium channel patches. Further, the delay between the onset of stimulation and a burst of exocytosis was prolonged for several seconds by increasing the concentration of the slow calcium chelator EGTA from 1.5 to 5 mM. These results demonstrate that while calcium channels and release sites tend to congregate in specialized regions of the surface membrane, these have dimensions of several micrometres. The dominant calcium signal regulating release in chromaffin cells is generated by the cooperative action of many channels operating over distances of many micrometres rather than discrete clusters of calcium channels generating localized microdomains.

(Resubmitted 27 May 2009; accepted after revision 10 September 2009; first published online 14 September 2009)
Corresponding author L. Lagnado: MRC Laboratory of Molecular Biology, Hills Road, Cambridge CB2 2QH, UK.
Email: ll1@mrc-lmb.cam.ac.uk

Abbreviations IRM, interference reflection microscopy; TIRFM, total internal reflection fluorescence microscopy.

Introduction

It is unclear how secretion in neuroendocrine cells is coupled to the opening of Ca^{2+} channels. One view is that a docked vesicle is triggered to fuse by a nearby 'Ca^{2+} microdomain' generated around a tight cluster of open Ca^{2+} channels (Olivos Ore & Artalejo, 2004), leading to the suggestion that excitation–secretion coupling in neuroendocrine cells is similar to synapses, where vesicles and Ca^{2+} channels cluster tightly at active zones (Cohen *et al.* 1991; Zenisek *et al.* 2003; Beaumont *et al.* 2005). However, this view is difficult to square with the functional and morphological differences in excitation–secretion coupling at synapses and endocrine cells. At synapses, vesicles begin fusing < 1 ms after Ca^{2+} channels open in response to an action potential (Robitaille *et al.* 1990; Cohen *et al.* 1991), while secretion in neuroendocrine cells is at least 100-fold slower (Almers, 1990; Martin, 1994; Zhou & Misler, 1995). Further, amperometry and capacitance experiments testing the effects of Ca^{2+} buffers indicate that delayed secretion is due to Ca^{2+} diffusion over distances of micrometres between Ca^{2+} channels and release sites (Chow *et al.* 1994, 1996).

The spatial organization of the secretory machinery in synapses is also very different to that in neuroendocrine cells. Fast release of neurotransmitter occurs at specialized active zones a few hundred nanometres in diameter where synaptic vesicles are tightly docked to the surface membrane prior to fusion. In contrast, docked granules in chromaffin cells display mobility within a 220 nm cage when unprimed and only become immobile after priming has taken place (Nofal *et al.* 2007). The structure organizing calcium channels in a synaptic terminal is the active zone (Khimich *et al.* 2005; Schoch & Gundelfinger, 2006; Long *et al.* 2008), but these are not observed in neuroendocrine cells. It is not clear, therefore, whether one might expect the same spatial organization of calcium signal and fusion site in neuroendocrine cells and synapses.

M. M. Wu and A. Llobet contributed equally to this work.

DOI: 10.1113/jphysiol.2009.176065

To understand excitation–secretion coupling in neuroendocrine cells, the submembranous Ca^{2+} signal should be compared with the spatial distribution of release sites. While Ca^{2+} microdomains have been visualized at synapses (Cohen *et al.* 1991; Tucker & Fettiplace, 1996; Zenisek *et al.* 2003; Beaumont *et al.* 2005), they have not been clearly demonstrated in neuroendocrine cells. Pulsed-laser imaging and amperometry were used to monitor Ca^{2+} influx and exocytosis in chromaffin cells and the results indicated that these processes tend to occur in similar regions of the membrane, although the spatial resolution did not allow detection of Ca^{2+} microdomains or 'active zones' of exocytosis (Robinson *et al.* 1995). A technique that provides better spatial resolution for detecting calcium influx at the membrane is total internal reflection fluorescence microscopy (TIRFM) (Zenisek *et al.* 2003; Beaumont *et al.* 2005; Demuro & Parker, 2006; Serulle *et al.* 2007). Becherer *et al.* (2003) applied TIRFM to chromaffin cells and inferred the existence of microdomains from local spikes in the noisy Ca^{2+} signal, but the stimulus they used – depolarization for several seconds by application of high K^+ – did not allow spatial calcium microdomains to be observed. We therefore set out to visualize calcium influx in chromaffin cells by using TIRFM to monitor calcium signals generated by very brief (2 ms) stimuli. Sites of granule fusion in the same region of membrane were then mapped using interference reflection microscopy (IRM; Llobet *et al.* 2008). The results we present demonstrate that while Ca^{2+} channels and release sites tend to occupy the same region of membrane, they are not tightly coupled in space. Excitation–secretion coupling in chromaffin cells therefore stands in contrast to synapses, where Ca^{2+} channels form tight clusters at the active zone (Cohen *et al.* 1991; Tucker & Fettiplace, 1996; Zenisek *et al.* 2003; Beaumont *et al.* 2005; Neher & Sakaba, 2008).

Methods

Cell preparation and solutions

Bovine adrenal chromaffin cells were prepared as described by Seward & Nowycky (1996). Adrenal glands were obtained from a local slaughterhouse and chromaffin cells isolated by collagenase digestion followed by purification using a Percoll gradient. Cells were plated onto poly-L-lysine-coated coverslips and used 1–3 days after preparation. Ringer solution contained (in mM): 140 NaCl, 2.5 KCl, 1 $MgCl_2$, 10 Hepes, 10 glucose, 2.5 $CaCl_2$, pH 7.4, 300 mosmol kg^{-1}. For TIRFM experiments 1 nM tetrodotoxin (Tocris, Ellisville, MO, USA) was added to Ringer solution. Nifedipine was from Sigma (St Louis, MO, USA), nimodipine from EMD Biosciences (San Diego, CA, USA); ω-agatoxin IVA and ω-conotoxin GVIA were from Alomone Labs (Jerusalem, Israel). Solutions were perfused onto cells using an array of quartz pipes (World Precision Instruments, Sarasota, FL, USA) controlled by a system of valves (Warner Instrument Corp., Hamden, CT, USA). The solution in the patch pipette contained (in mM): 120 caesium methanesulfonate, 10 TEA-Cl, 5 $MgCl_2$, 20 Hepes, 3 Na_2ATP, and 1 NaGTP, pH 7.2, 290 mosmol kg^{-1}. For IRM experiments, the pipette solution contained variable amounts of Ca^{2+} buffer, either (in mM) 0.1 EGTA, 1.5 EGTA, 5 EGTA or 0.4 BAPTA. For TIRFM experiments, pipette solution contained either 0.1 mM OregonGreen488-BAPTA-2 ($K_d = 0.6\ \mu$M; OGBAPTA-2) or 0.2 mM Fluo-5N ($K_d = 90\ \mu$M; Molecular Probes, Eugene, OR, USA).

Electrophysiology and imaging

IRM imaging was performed as described previously (Llobet *et al.* 2003; Beaumont *et al.* 2005). Cells were voltage clamped in the whole-cell configuration using an Axopatch 200A amplifier (Axon Instruments, Union City, CA, USA) and acquired with a G4 Macintosh equipped with an ITC-16 interface (Instrutech Corp., Port Washington, NY, USA) controlled by the Pulse Control extension (Herrington & Bookman, 1994) of IGOR Pro software (Wavemetrics, Lake Oswego, OR, USA). Exocytosis was elicited by depolarizing from −80 mV to +10 mV, either as a single 500 ms step or as a train of 24×105 ms or 4×90 ms pulses. We used 105 ms pulses to allow each to be delivered at the beginning of a frame acquired by the camera. Image acquisition was performed using IPLab software and triggered by a TTL pulse delivered by the ITC-16 at the beginning of the electrophysiological recording. Calcium currents were leak subtracted using macros written in IGOR Pro. All IRM images and movies were 'background subtracted' using a macro written in IPLab (Scanalytics, Fairfax, VA, USA) to better visualize changes.

'Through the objective' TIRFM was combined with IRM as described (Llobet *et al.* 2003; Beaumont *et al.* 2005). A 488 nm beam from an argon laser provided the TIRFM excitation light. The light for IRM originated from a 100 W xenon lamp (Newport-Oriel, Irvine, CA, USA) and was transmitted through a 510WB40 filter (Omega Optical, Brattleboro, VT, USA) before passing through a combining cube (Oriel). The filter block contained a 505DRLP dichroic (Omega), which reflected >95% at 488 nm and about 35% at 510 nm, while transmitting > 80% at wavelengths > 515 nm. About 35% reflection was sufficient for IRM if the xenon lamp was at maximum power. When only TIRFM was used, emitted light was filtered through a HQ510LP filter (Chroma Technology, Rockingham, VT, USA) and 488 nm notch filter (Coherent, Santa Clara, CA, USA). When TIRFM was combined with IRM, emitted light was filtered through a 545AF75 filter (Omega). Images were magnified × 2.2 before being acquired by a Princeton Instruments Pentamax CCD camera and Winview32

acquisition software (Roper Scientific, Trenton, NJ, USA). Image acquisition was synchronized with the electrophysiological recording using a Master-8 pulse generator (AMPI, Jerusalem, Israel). The membrane current and camera exposure signal time were digitized (20 kHz) and filtered (5 kHz) by a Digidata 1322A interface (Axon).

Images of Ca^{2+} influx in Figs 4–9 are shown as $\Delta F/F_0$, where $\Delta F = F - F_0$, F is the individual frame and F_0 is the average image at rest (obtained from between 4 and 15 consecutive frames acquired before the stimulus). The protocol for identifying sites of calcium influx by TIRFM is described further in Supplemental Fig. 2. To quantify changes in Ca^{2+} influx between different stimulus trains (Figs 8 and 9), we compared ΔF values measured in the frame in which the 2 ms stimulus was applied. Each pixel from the ΔF image obtained after adding a blocker of Ca^{2+} channels was divided by the corresponding pixel in the ΔF image obtained before addition of the blocker. The ratio values for each pixel within the Ca^{2+} channel patch were then averaged to give the mean intensity ratio (± S.D.) over all pixels in the patch. The ratio image of Stim 2/Stim 1 therefore provided a measure of the relative change in the amount of Ca^{2+} influx in the footprint. Measurements of the free $[Ca^{2+}]$ under the membrane using Fluo-5N were calibrated (Fig. 3) by measuring F_{min} in pipette solution containing 10 mM EGTA and F_{max} in pipette solution containing 1 mM $CaCl_2$. The K_d for Fluo-5N was assumed to be 90 μM, measured by the manufacturers. Results are expressed as mean ± S.E.M. unless otherwise indicated.

Results

Using IRM to detect fusion of large dense-core vesicles

To investigate excitation–secretion coupling in chromaffin cells we visualized sites of fusion using IRM, a technique that detects local invaginations of the surface membrane generated by fusion of a vesicle. Examples of such events are shown in Fig. 1*A* and *B*, where they appear as localized 'spots' within the footprint of the cell (see Movie 1 in Supplemental material, available online only). A large number of experimental observations indicate that these spots are generated by the Ω-shapes formed when a vesicle fuses with the surface membrane (Llobet *et al.* 2003, 2008). First, spots in the footprint only occur during and after the application of a depolarizing stimulus. Second, they are synchronized in time and space with the release of FM4-64, acridine orange or pro-atrial natriuretic peptide (ANP)-GFP within granules, as visualized by simultaneous TIRFM and IRM imaging. Third, the number of events in a footprint is directly proportional to the total increase in surface area measured by the capacitance technique and follows the same time course. Fourth, the average capacitance increase per event is 1.43 fF, which is very similar to the average capacitance of a granule estimated by Ales *et al.* (1999). Fifth, the kinetics of IRM signals are altered by a number of experimental manipulations known to affect the fusion or retrieval of granules. For instance, the speed of IRM signals are calcium dependent: recovery of the signal is blocked by strontium, which also blocks vesicle retrieval assayed by capacitance (Llobet *et al.* 2008). The full procedure by which IRM was used to identify the timing and location of

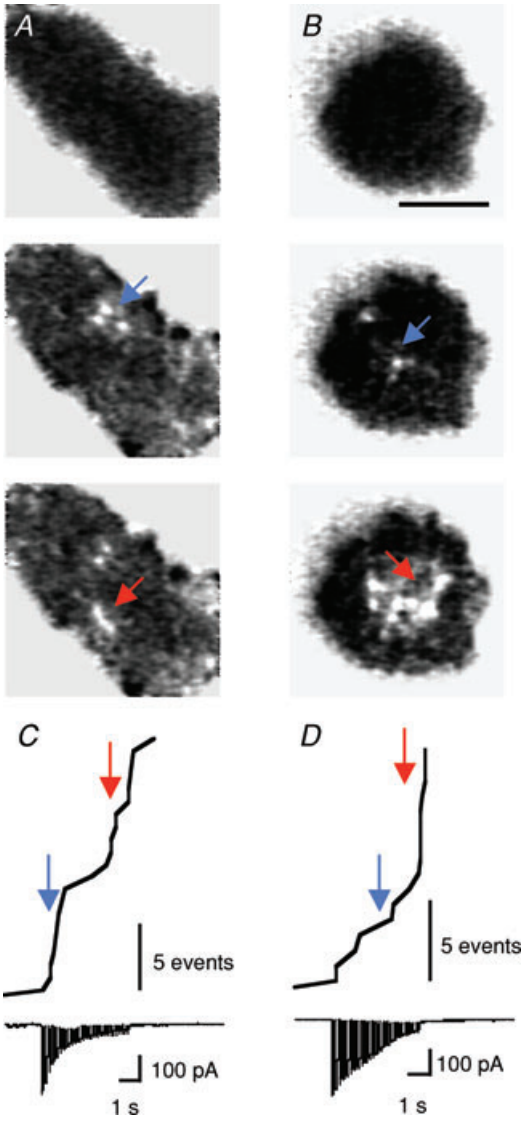

Figure 1. Bursts of fusion events occurring in clusters on the membrane
A and *B*, background-subtracted IRM images from 2 different cells stimulated with a train of 24 × 105 ms depolarizations at 5 Hz. Before stimulation, IRM footprints were uniformly dark (top row), but discrete spots appear on depolarization. *A* was recorded with 1.5 mM EGTA in the patch pipette and *B* with 5 mM EGTA. Image in *B* comes from Supplemental Movie 1, available online only. Scale bar, 5 μm. *C* and *D*, the cumulative number of fusion events and the corresponding whole-cell Ca^{2+} currents plotted for cells in *A* and *B*. Coloured arrows correspond to time points at which the frames shown in *A* and *B* were extracted. Note the slower inactivation of Ca^{2+} currents in *D* compared to *C*. Scale bar, 5 fusion events.

fused granules is described in the online 'Supplementary Information' and Supplemental Fig. 1.

Bursts of exocytosis were delayed by EGTA

When a chromaffin cell was depolarized, fusion events within the footprint often occurred in bursts, and the timing of these depended on the concentration of the Ca^{2+} chelator inside the whole-cell pipette. The cell in Fig. 1*A* was dialysed with 1.5 mM EGTA, which binds Ca^{2+} ions with a K_d of ~150 nM. While Ca^{2+} channels were closed, there was no activity (top), but a stimulus train lasting 5 s triggered the appearance of discrete bright spots. A cumulative plot of fusion events shows that exocytosis in this footprint occurred in two distinct bursts, the first complete within 1 s of the beginning of the stimulus train and the second occurring more slowly over a period of several seconds (Fig. 1*C*). Two phases of exocytosis are also observed in chromaffin cells using the capacitance technique and release of caged Ca^{2+}: the initial exocytic burst is complete within a few hundred milliseconds at 10–20 μM Ca^{2+} and the second occurs at a rate of 0.1 s^{-1} (Xu *et al.* 1998). In comparison, we estimated that the $[Ca^{2+}]$ within ~100 nm of the membrane reached ~20–30 μM during depolarization under conditions of low Ca^{2+} buffering (Fig. 7).

When the concentration of EGTA inside the pipette was increased from 1.5 mM to 5 mM, the initial rate of exocytosis was slowed (Fig. 1*D*). Averaged time courses of exocytosis in 0.1 mM, 1.5 mM and 5 mM EGTA are shown by the cumulative histograms in Fig. 2*A*–*C*. Each plot is averaged from 4–5 footprints, and was obtained by making cumulative histograms of all events under each condition, then dividing by the number of footprints from which these measurements were collected. The initial rates of granule fusion were then compared by making linear

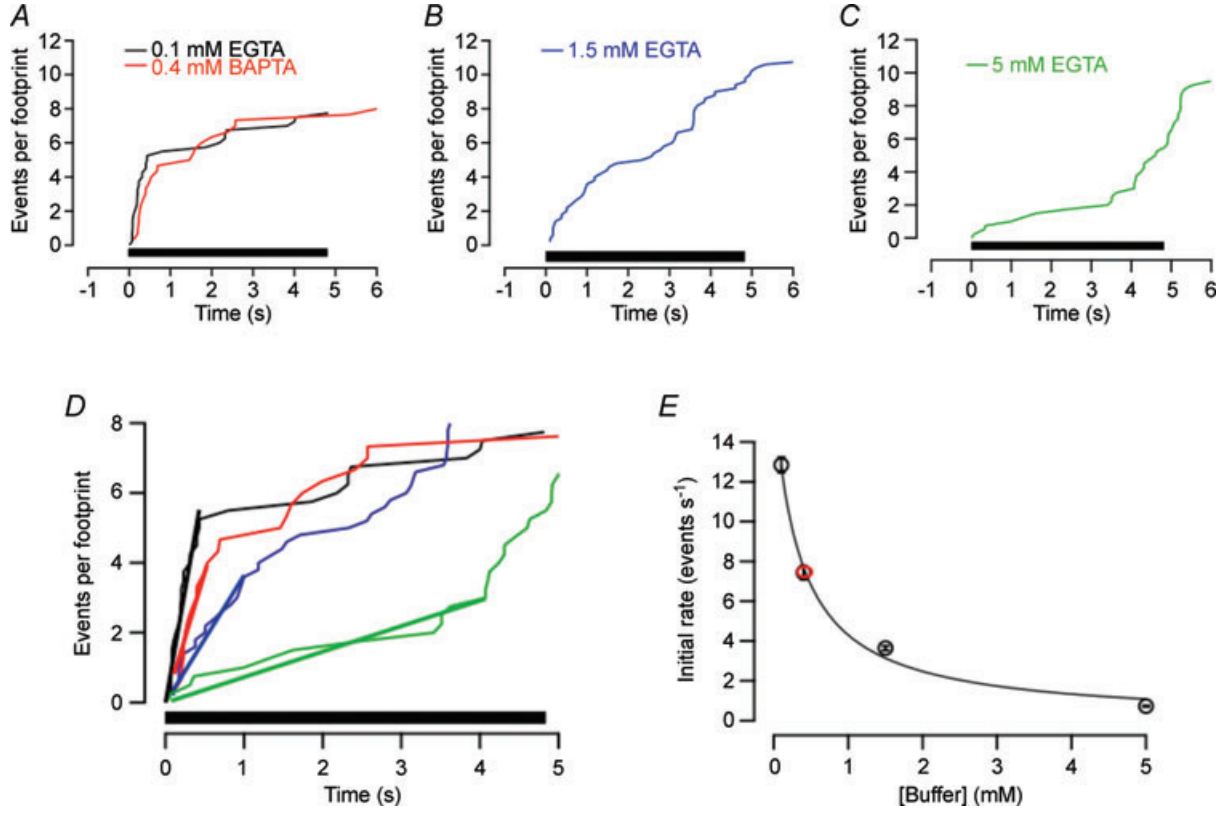

Figure 2. EGTA increased the delay between the beginning of stimulation and the first burst of exocytosis

A–*C*, cumulative plot of number of fusion events per footprint observed during trains of 24 × 105 ms depolarizations delivered at 5 Hz. Cells were dialysed with 0.1 mM EGTA (*A*; $n = 4$), 1.5 mM EGTA (*B*; $n = 5$), 5 mM EGTA (*C*; $n = 4$) or 0.4 mM BAPTA (*A*; $n = 3$). *D*, the traces in *A*–*C* superimposed on an expanded time scale. The initial phases of release have been fitted with straight lines through the origin (bold). *E*, the initial rate of fusion events (per second per footprint) as a function of the concentration of EGTA or BAPTA in the patch pipette. The line through the points is the least-squares fit of the relation $R = R_{max}[1 - (E/(E + E_{1/2}))]$, where E is the concentration of buffer in mM, $E_{1/2}$ is the concentration where inhibition is half-maximal (0.36 mM) and R_{max} is the maximum rate of release in the absence of any calcium buffer in the patch pipette (16 events per second per footprint). Both R_{max} and $E_{1/2}$ were free parameters in the fitting process. The red point is a measurement in BAPTA and the black points are measurements in EGTA. Error bars show the standard deviation of the linear fits in *D* (some of these are narrower than the points).

fits to the cumulative histograms (bold lines in Fig. 2*D*). Under these stimulation conditions, the frequency of fusion events was sensitive to EGTA, as would be expected from capacitance measurements (Moser & Neher, 1997). The initial rate of fusion in 0.1 mM EGTA was sevenfold higher than in 5 mM EGTA (Fig. 2*D*), but there was still an obvious burst of exocytosis in 5 mM EGTA; the crucial difference was that the most rapid phase of fusion in 5 mM EGTA was delayed by 3–4 s. In other words, the slowing of exocytosis by EGTA could be overcome by more prolonged Ca^{2+} influx. This observation argues strongly against the idea that the signal triggering granule fusion is a localized microdomain, for two reasons. First, both theory (Naraghi & Neher, 1997) and experimental measurements (Zenisek *et al.* 2003; Beaumont *et al.* 2005) demonstrate that Ca^{2+} microdomains persist in EGTA concentrations up to 5 mM, because this chelator binds Ca^{2+} ions relatively slowly. The major effect of EGTA is to suppress the 'global' increase in Ca^{2+} generated by diffusion of Ca^{2+} away from sites of influx (Zenisek *et al.* 2003; Beaumont *et al.* 2005). Second, Ca^{2+} microdomains are generated within milliseconds when Ca^{2+} channels open, even in the presence of high concentrations of EGTA (Zenisek *et al.* 2003). The delayed burst of exocytosis in 5 mM EGTA must therefore reflect the gradual accumulation of free Ca^{2+} ions some distance from calcium channels.

Secretion triggered by calcium microdomains at the synapse can be inhibited much more efficiently by the Ca^{2+} chelator BAPTA compared to EGTA (Adler *et al.* 1991; Burrone *et al.* 2002). BAPTA binds Ca^{2+} ions with a similar affinity to EGTA but about 60-fold faster, and therefore has a stronger effect on calcium signals close to calcium channels (Neher, 1998). To compare the effects of these buffers on granule fusion in chromaffin cells, we first looked at the relation between the initial rate of fusion and the EGTA concentration, shown by the black circles in Fig. 2*E*. These measurements could be described empirically by a function assuming that EGTA inhibits granule fusion according to the relation $R = R_{max}[1 - (E/(E + E_{1/2}))]$, where E is the concentration of EGTA in mM, $E_{1/2}$ is the concentration where inhibition is half-maximal (0.36 mM) and R_{max} is 16 events per second per footprint. To test whether BAPTA was any more effective than EGTA at slowing granule fusion, we introduced 0.4 mM BAPTA, which would be expected to have an effect that was approximately half-maximal if the two chelators were equally effective at antagonizing granule fusion (Fig. 2*E*). The red point in Fig. 2*E* shows that BAPTA was not significantly more, or less, effective than EGTA. This observation indicates that the equilibrium dissociation constant of these chelators is more important than the association constant for Ca^{2+} binding in inhibiting granule fusion, and that this process is therefore triggered by the global increase in $[Ca^{2+}]$ rather than Ca^{2+} microdomains.

Repeated fusion events at specialized sites

At some sites in the membrane, fusion events occurred repeatedly during a train of stimuli lasting 5 s. Figure 3*A* and *B* shows examples of two cells which were stimulated twice, and the arrows identify fusion events which occurred in the same spot in the separate stimuli (see also online Supplemental Movie 2). Of 307 fusion events in 12 cells stimulated 3–6 times, 115 occurred within one pixel of each other (the centre of the event being defined as the pixel in which the IRM signal was at its maximum and each pixel being 73 nm square). In some cases, different fusion events occurred centred over the same pixel three

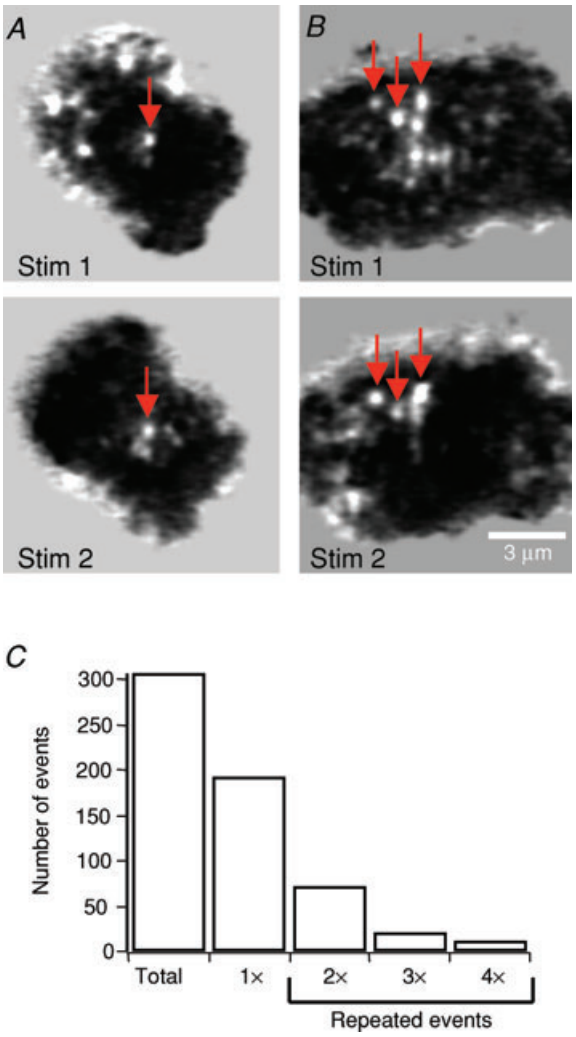

Figure 3. Specialized sites of fusion
A and *B*, background-subtracted images from the IRM movies of two cells, each stimulated twice (Stim 1 and Stim 2). Arrows are located in the same position during the first and second stimulations, indicating fusion events occurring in the same spot. Stim 1 and Stim 2 images in *B* are from Supplemental Movie 2 (available online only). *C*, histogram showing the number of fusion events that occurred within the same spots two, three, or four times, from a total of 307 events. The bar marked '1×' is the number of events that did not overlap with any others.

or more times (Fig. 3*C*). Thus at least 37% of fusion events occurred at sites that were fixed in the membrane over the tens of minutes time scale of these experiments. This figure will be a lower limit because the relatively low average release probability at a single site would have required many repetitive stimuli to identify all the preferred sites in this way. Nonetheless, these results indicate that the membrane of chromaffin cells contains areas at which vesicles can fuse repeatedly. Clustering of multiple fusions in a single site could be due to the sequential arrival of different granules to preferential release zones of $\sim$0.4 μm^2 (Rickman *et al.* 2004; Kishimoto *et al.* 2006) and/or to a small granule population undergoing repeated cycles of fusion and re-sealing in a circumscribed portion of the membrane (Perrais *et al.* 2004).

Calcium influx occurred in large patches

We next sought to investigate how sites of fusion were organized spatially relative to Ca^{2+} channels in the membrane, and in particular whether depolarization generated discrete calcium microdomains or more diffuse signals. Submembranous Ca^{2+} was imaged by TIRFM using the indicator OGBAPTA-2 (0.1 mM). At the synapse of goldfish retinal bipolar cells, Ca^{2+} microdomains generated by tight clusters of Ca^{2+} channels can be clearly visualized after depolarizations lasting 20 ms (Zenisek *et al.* 2003; Beaumont *et al.* 2005). We sought to capture an even briefer 'snap-shot' of Ca^{2+} entry in chromaffin cells by depolarizing for just 2 ms and integrating the signal over a single frame lasting 11 ms. This stimulus moved a Ca^{2+} charge of 0.9 ± 0.1 pC into the cell, similar to the $\sim$1 pC delivered in response to a single action potential (Giovannucci *et al.* 1999). The resulting calcium signal is shown in Fig. 4*A*, which is a series of 5 out of 7 consecutive frames, with the depolarization delivered at the beginning of frame 5. Calcium influx was not uniform across the footprint, but occurred in distinct patches. Then, after Ca^{2+} channels closed, the fluorescence gradually dissipated as Ca^{2+} diffused away from entry sites (Fig. 4*A*, frames 6 and 7). The source of Ca^{2+} influx was a relatively fixed array of channels because when the depolarization was repeated (Fig. 4*B*), the submembranous Ca^{2+} signal was similar for each of five stimuli (Fig. 4*C*). Calcium influx therefore occurred diffusely rather than in discrete puncta. Calcium influx visualized by TIRFM is also shown in Supplemental Movies 3 and 4.

Might these 'patchy' Ca^{2+} signals reflect non-uniform attachment of the footprint to the glass coverslip? Three observations argue against this possibility. First, the IRM experiments showed that footprints presented a homogeneous pattern of interference before stimulation (Fig. 1*A* and *B*). Moreover, signals arising exclusively from the edges of the footprint were not considered because these were the membrane regions that tended to display a looser attachment to the coverslip. Second, the fluorescence intensity of OGBAPTA-2 viewed by TIRF was relatively uniform across the footprint at resting levels of Ca^{2+} (Fig. 5 below). And, third, the submembranous Ca^{2+} signal measured by TIRFM was also relatively uniform when a large Ca^{2+} load was introduced and allowed to dissipate after closure of Ca^{2+} channels. An example of this behaviour can be seen in Fig. 7*A*, where there is a patchy Ca^{2+} signal evident during the first depolarization of a train (frame 29), but a much more uniform signal after closure of Ca^{2+} channels at the end of the train (frame 36). We conclude that the patchy signals reported by OGBAPTA-2 reflected the distribution of calcium channels in the surface membrane.

Measuring areas of calcium influx

The area covered by arrays of Ca^{2+} channels varied widely. Two relatively localized Ca^{2+} signals, indicating a small cluster of Ca^{2+} channels, are shown by the red arrows in Fig. 4*A*. These signals might be termed 'microdomains' because their spatial scale is 1–2 μm (Neher & Sakaba, 2008), but the predominant signal was much more widely distributed. The areas of Ca^{2+} influx in the footprints of ten other cells are shown in Fig. 4*D*. Surveying these examples, it is possible to see 'hotspots' within the larger regions of Ca^{2+} influx, indicating that the density of Ca^{2+} channels per unit area was not necessarily uniform across these patches. The basic observation was that independent microdomains (such as arrowed in Fig. 4*A*) were rare, and the predominant Ca^{2+} signal was distributed over much wider regions. These patches of Ca^{2+} influx were relatively well circumscribed and their boundaries could be recognized by eye (Fig. 4*D*).

To measure the areas of the footprint and patches of Ca^{2+} influx we applied a thresholding technique. Figure 5*A* shows the resting fluorescence of a chromaffin cell loaded with 0.1 mM OGBAPTA-2 (left). To allow imaging at 11 ms per frame, we sampled a 50 pixels $\times$ 50 pixels region of interest (ROI). The minimum and maximum pixel intensities for the first frame in a movie were measured (MIN_{frame1} and MAX_{frame1}), and a threshold set at 20% of the total intensity range (i.e. $MIN_{frame1} + 0.2(MAX_{frame1} - MIN_{frame1})$). This thresholding criterion was chosen as one which effectively separated the footprint from the background signal over the neighbouring coverslip. An example is shown in Fig. 5*A*, where all pixels below the threshold are marked in red (middle), and the margins of these regions, marking the outline of the footprint, are shown by the lines in the image on the right. Similar criteria were applied to define patches of Ca^{2+} influx. Figure 5*B* shows the relative change in the fluorescence of OGBAPTA-2 in the frame in which Ca^{2+} influx was activated for 2 ms (left). First

we determined the maximum pixel intensity over all the prestimulus frames ($MAX_{frame1-4}$), then the maximum pixel intensity of the stimulus frame (MAX_{frame5}). The minimum threshold was set at 20% of this range (i.e. $MAX_{frame1-4} + 0.2(MAX_{frame5} - MAX_{frame1-4})$). The pixels above this threshold are marked in green in the middle panel in Fig. 5*B*, and the margins of the contiguous area are shown by the green line in the right panel. The size of the Ca^{2+} channel arrays ranged from 10 to 78 μm^2, with a mean size of ~34 μm^2. On average there were two distinct patches per footprint.

Exocytosis within patches of calcium channels

The results presented in Figs 1, 3 and 5 indicated that clusters of fusion events occurred on spatial scales similar to patches of Ca^{2+} channels. To determine more precisely where exocytosis occurred relative to Ca^{2+} channels, we applied IRM and TIRFM in the same cells. Three examples are shown in Fig. 6*A*–*C*. First, the IRM images at the top were obtained by integrating over a period of 12 s from the onset of the stimulus, which was delivered in the perforated patch configuration. The longer integration time compared to Fig. 1 provided a view of all the sites where granules fused over this period, and the brighter white spots reflect sites where two or more fusion events occurred (as assessed by observing the movie of difference images frame by frame, as shown in Fig. 1). The corresponding TIRFM images at the bottom show Ca^{2+} channel patches visualized in the same footprint by going whole-cell with the pipette containing 0.1 mM OGBAPTA-2. Overlaid onto the Ca^{2+} channel patches

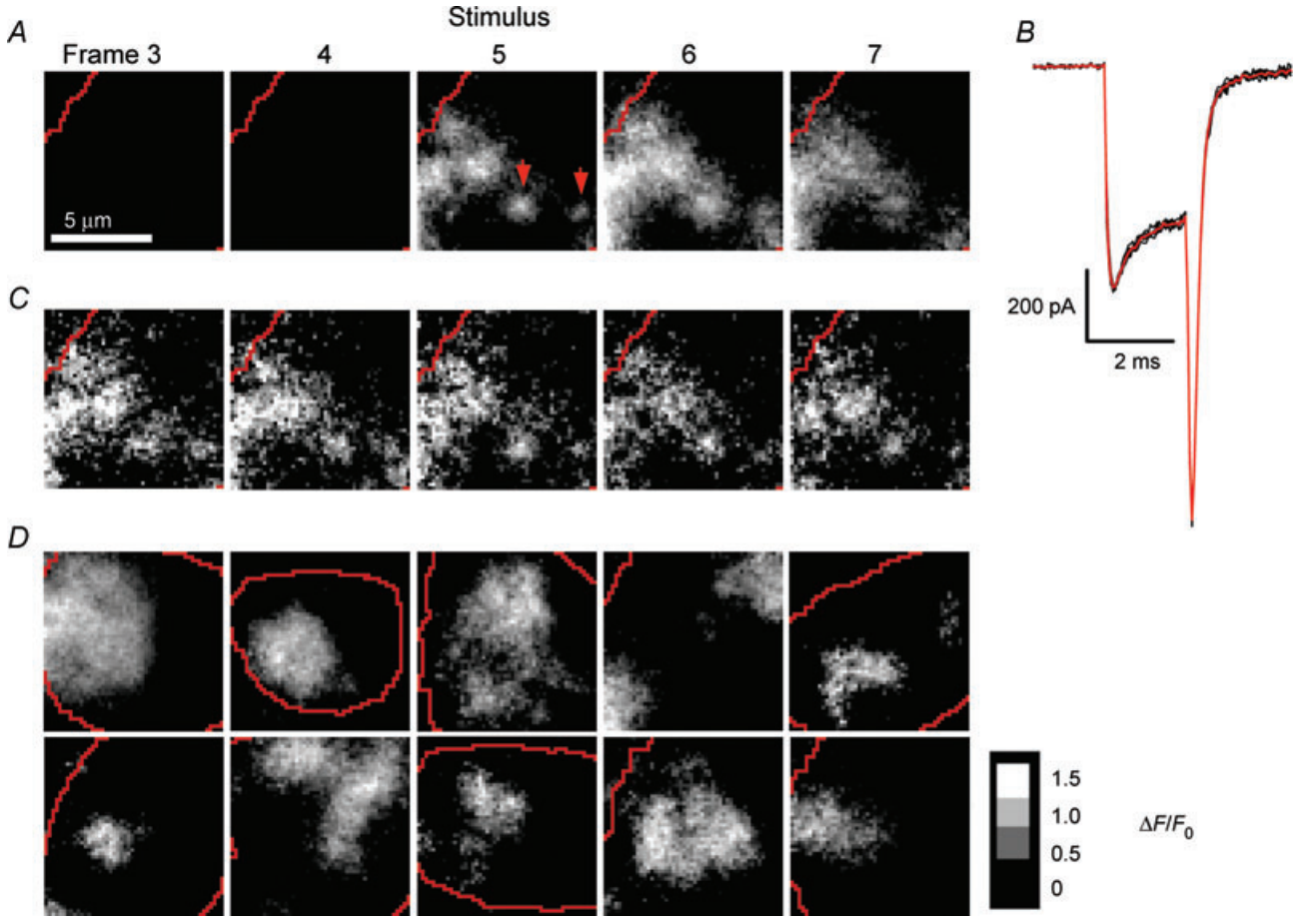

Figure 4. Visualizing sites of calcium influx by TIRFM
A, images showing the relative change in fluorescence ($\Delta F/F$) of OGBAPTA-2 (0.1 mM) in the footprint of a chromaffin cell. Averaged from six movies of 7 × 11 ms frames acquired at 10 s intervals, all from the same cell. Calcium influx was triggered by a 2 ms depolarization (−80 to +10mV) delivered at the beginning of frame 5; a 1 ms prepulse from −80 mV to +150 mV was delivered immediately preceding the 2 ms depolarization. Red lines indicate the edges of the footprint. *B*, whole-cell Ca^{2+} currents recorded for each of the 6 stimuli delivered to the cell in *A* (black traces) and the average of the 6 traces (red). *C*, five individual examples of the stimulus frames used to make the averaged frame 5 in *A*. *D*, a gallery of averaged stimulus frames showing the relative change in intensity ($\Delta I/I_0$) from 10 different cells on a grey scale. Each image is the average of 6 or 8 stimulus frames. Scale bar in arbitrary units shows $\Delta I/I_0$.

are yellow and blue spots marking the sites of fusion events occurring during the stimulus (synchronous) and after the stimulus (asynchronous), identified from the IRM movies. Most sites of fusion were within the large regions of the surface membrane containing Ca^{2+} channels.

To determine whether fusion events occurred preferentially within the Ca^{2+} channel patches, we measured the area of the footprint (A_{foot}) and the area covered by patches of Ca^{2+} channels (A_{patch}) for each cell ($n = 10$). If all of the fusion events visualized under IRM ($N_{total} = 137$ events) were randomly distributed across the footprint, then the predicted number of fusion events within A_{patch} would be: $N_{predict} = (A_{patch}/A_{foot}) \times N_{total}$. The actual number of fusion events occurring within the Ca^{2+} channel patch (N_{actual}) was compared to $N_{predict}$ for each cell. The total N_{actual} was 109 events, significantly larger ($P = 0.01$, Student's paired, two-tailed t test) than the total $N_{predict}$ of 92 events. In 70% of the cells, $N_{actual} > N_{predict}$, while in the remaining 30% $N_{actual} = N_{predict}$. These results confirmed that fusion events in the footprints of chromaffin cells were not randomly distributed but occurred preferentially within patches of Ca^{2+} channels.

Might the clustering of fusion events within Ca^{2+} channel patches simply reflect the higher local Ca^{2+} concentration? Two observations argued against this possibility. First, while most fusion sites occurred in regions of the surface membrane containing Ca^{2+} channels, several were towards the margins of these patches (e.g. Fig. 6*A*) and 20% outside (e.g. Fig. 6*B*). Second, when we analysed all the fusion events in 10 cells, we found that asynchronous events also occurred preferentially within patches of Ca^{2+} channels (Fig. 6*D*). These results indicate that the local Ca^{2+} concentration was not the only factor causing fusion to occur preferentially in regions of the surface membrane containing Ca^{2+} channels. It seems most likely that greater numbers of vesicles were docked in these areas or that the vesicles were better primed for release.

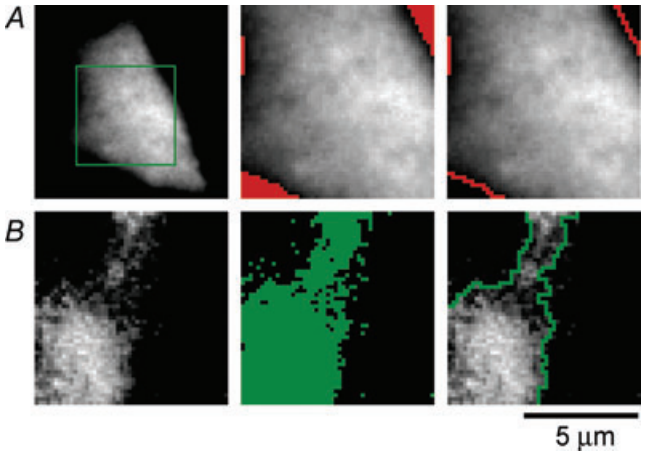

Figure 5. Defining the area of the footprint and calcium patches
A, defining the area of the footprint. TIRFM image of a voltage-clamped chromaffin cell, at rest, loaded with 0.1 mM OGBAPTA-2. To acquire TIRFM images at 11 ms per frame, data collection was restricted to a 50 pixels × 50 pixels ROI (green box, left). To define the outline of the footprint, we determined the minimum (MIN_{frame1}) and maximum (MAX_{frame1}) pixel intensities for the first frame in a movie. A threshold was then set at the minimum pixel intensity (MIN_{frame1}) + 20% of the total intensity range (MAX_{frame1}) – (MIN_{frame1}). All pixels below the threshold are marked in red (middle), and the margins of these regions are shown by the lines in image at right. *B*, defining the area of calcium influx. An image of the relative change in the fluorescence of OGBAPTA-2 ($\Delta F/F$) in the frame in which Ca^{2+} influx was activated for 2 ms is shown at left. This image was thresholded by first determining the maximum pixel intensity over all the prestimulus frames ($MAX_{frame1-4}$) and the maximum pixel intensity of the stimulus frame (MAX_{frame5}). The minimum threshold was set as ($MAX_{frame1-4}$) + 20% of the intensity range (MAX_{frame5}) – ($MAX_{frame1-4}$). The pixels above this threshold are marked in green in the middle panel and the margins of this area are shown by the green line in the right panel.

The calcium signal triggering synchronous and asynchronous fusion events

The stimulus we used to visualize the distribution of Ca^{2+} channels – a depolarization lasting 2 ms – was too brief to trigger exocytosis. To better understand excitation–secretion coupling we therefore also imaged the submembranous Ca^{2+} signal during more prolonged Ca^{2+} influx sufficient to trigger exocytosis, using trains of 4 × 90 ms depolarizations. Fluo-5N was used as the Ca^{2+} indicator because its relatively low affinity ($K_d = 90\ \mu M$) prevented saturation in the face of these much larger Ca^{2+} loads. Figure 7*A* shows a series of consecutive frames lasting 100 ms, with 90 ms depolarizations delivered during frames 29, 31, 33 and 35. Patches of Ca^{2+} channels could be recognized in response to the first stimulus in the train (frame 29), but diffusion of Ca^{2+} from these regions caused a gradual build-up under the whole membrane (compare frames 30 and 36). Figure 7*B* shows the submembranous Ca^{2+} concentration over the whole footprint (black) compared with two 10 pixels × 10 pixels ROIs, one within (green) and one outside (red) a patch of Ca^{2+} channels. Average Ca^{2+} levels reached a maximum of about 30 μM within the Ca^{2+} patch during the stimulus, but rapidly fell after closure of Ca^{2+} channels. Of a total of 137 fusion events, 43% occurred 1 s or more after Ca^{2+} influx had stopped, at Ca^{2+} concentrations below 6 μM (Fig. 7*B*). Clearly, exocytosis was not tightly coupled to the opening of Ca^{2+} channels. These results provide further evidence against the idea that fusion of secretory vesicles in chromaffin cells is driven by localized Ca^{2+} microdomains.

Calcium channel patches consisted primarily of N- and P/Q-type channels

Bovine adrenal chromaffin cells express three types of voltage-activated Ca^{2+} channels, N-, L- and P/Q-type (García *et al.* 2006). Several studies have examined the efficiency with which the different channel subtypes trigger exocytosis in chromaffin cells but with conflicting results (Artalejo *et al.* 1994; Lara *et al.* 1998; Gil *et al.* 2001). N- and P/Q-type channels contain a synprint region that allows interaction with syntaxin, SNAP-25, and synaptotagmin (Catterall, 1999); thus, these channels may localize to regions of the surface membrane where the SNARE complex has formed in preparation for fusion. We therefore compared how different subtypes of Ca^{2+} channels were distributed within and between patches.

After imaging sites of Ca^{2+} influx under normal conditions, we applied dihydropyridines (DHP) to block L-type channels, ω-conotoxin GVIA (CTX) to block N-type channels, or ω-agatoxin IVA (AGA) to block P/Q-type channels. The averaged responses to the first set of 2 ms stimuli under control conditions are shown in the top row in Fig. 8*A*–*D* ('Stim 1'); the response to the second set of stimuli under test conditions is shown in the middle row ('Stim 2'), and the ratio images of Stim 2/Stim 1 are at the bottom. When the second set of stimuli was also delivered in the absence of any pharmacological agents, the average ratio of (Stim 2/Stim 1) was one (Fig. 8*A*), indicating there was little change in Ca^{2+} influx between the two sets of stimuli (Fig. 8*A*, bottom). The (Stim 2/Stim 1) ratio was also equal to one after treatment with dihydropyridines, indicating that blocking L-type Ca^{2+} channels did not significantly decrease Ca^{2+} influx in the footprint, even though the whole-cell Ca^{2+} current was inhibited by 20% (Fig. 8*B*). In contrast, treatment with CTX resulted in an 80% decrease in Ca^{2+} influx between Stim 1 and Stim 2 (Fig. 8*C*), while application of AGA led to a 40% decrease (Fig. 8*D*). These results indicate that patches of Ca^{2+} channels within the footprint were made up primarily of N- and P/Q-types, with very few active L-type channels.

The ratio images (Stim 2/Stim 1) in Fig. 8*C* and *D* were relatively uniform, as they were in 13 other cells tested,

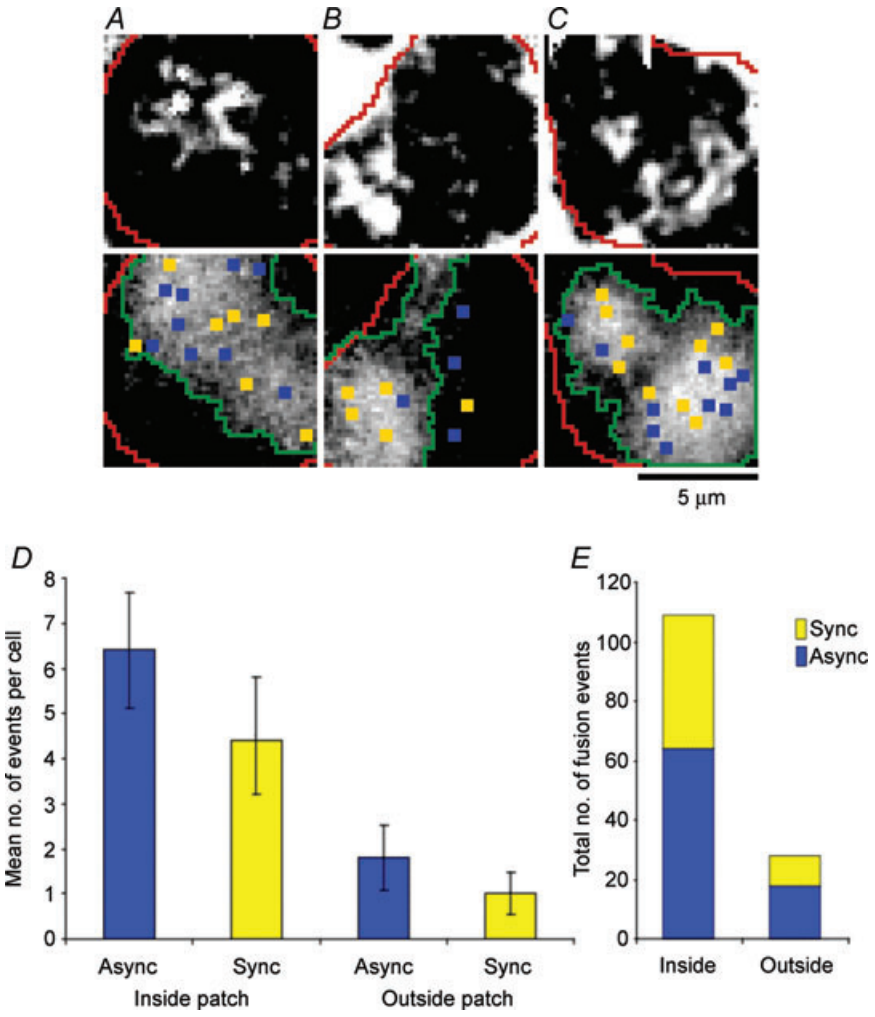

Figure 6. Fusion events occurred preferentially close to calcium channels
IRM images averaged over a 12 s period from the start of the stimulus are shown in the top row and areas of Ca^{2+} influx visualized by TIRFM are shown below for three different cells (*A*–*C*). To trigger the fusion events (*A*–*C*, top), cells were voltage clamped in the perforated-patch configuration and stimulated with 4 × 90 ms depolarizations at 5 Hz. We then broke-through to whole-cell configuration and loaded cells with 0.1 mM OGBAPTA-2. The TIRFM images of Ca^{2+} influx (*A*–*C*, bottom) show the average stimulus frames ($\Delta F/F$), as in Fig. 4*D*. Overlaid onto the TIRFM images are the sites of synchronous (yellow) and asynchronous (blue) fusion events visualized by IRM, the outline of the footprints (red lines), and the perimeter of the Ca^{2+} channel patches (green lines). *D*, average number, per cell, of asynchronous and synchronous fusion events occurring inside *vs.* outside of calcium channel patches. The differences between the means for asynchronous events inside *vs.* outside were significantly different (*t* test, $P = 0.006$), as were the differences between the means for synchronous events inside *vs.* outside ($P = 0.03$). Error bars are S.E.M.; $n = 10$ cells for each. *E*, total number of fusion events recorded for 10 cells (137 total events) is broken down to reveal the ratio of synchronous to asynchronous, inside and outside of the calcium channel patches.

indicating that the distributions of N- and P/Q-type channels were similar across a patch. Figure 8*E* compares how these blockers of Ca^{2+} channels affected the total amount of Ca^{2+} influx into the cell (measured as the integral of the Ca^{2+} current, *Q*) and the influx into the footprint (measured as the mean pixel intensity in the ratio image Stim 2/Stim 1). In cells treated with CTX and AGA, inhibition of the Ca^{2+} current was correlated with a decrease in the amount of Ca^{2+} entering through the footprint. In contrast, in cells treated with DHP, Ca^{2+} influx into the footprint was not significantly reduced. Thus, L-type channels were segregated away from N- and P/Q-type channels in the footprint. This conclusion was reinforced by successively blocking each Ca^{2+} channel subtype in the same cell. In the example in Fig. 9, applying DHP reduced the total Ca^{2+} current by about 70% (Fig. 9*B*), without any effect on the Ca^{2+} influx through the footprint (mean pixel intensity ratio of 0.99 ± 0.13 in Fig. 9*D*). When CTX was added in addition to DHP, the mean intensity ratio was 0.59 ± 0.12 (Fig. 9*F*), while further addition of AGA completely blocked Ca^{2+} influx (Fig. 9*H*). Thus the footprint contained only N- and P/Q-type channels, and the ratio images show that these were distributed relatively uniformly.

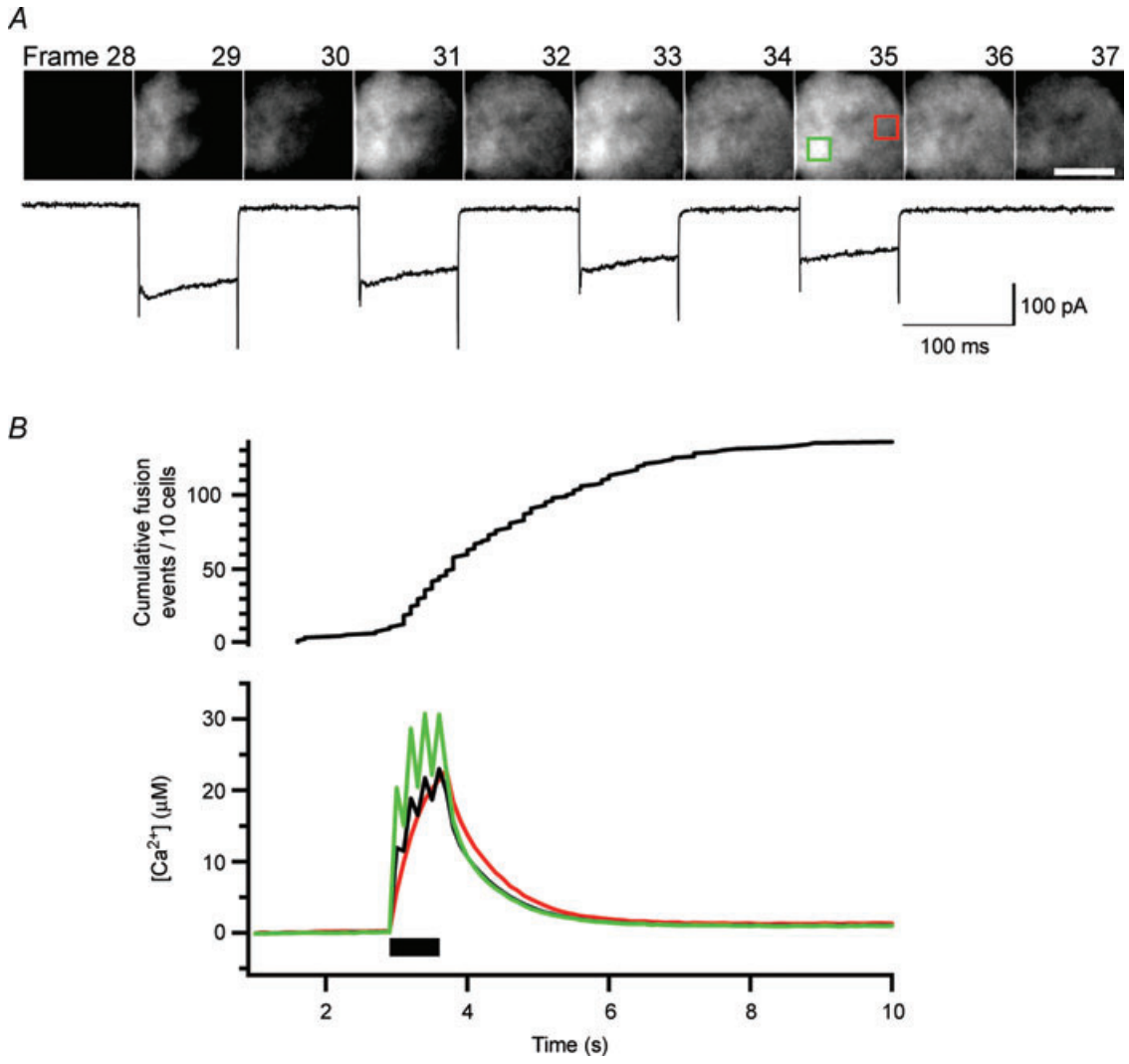

Figure 7. Visualizing calcium influx with a low affinity calcium indicator
A, ten consecutive frames showing $\Delta F/F$ from a cell loaded with 0.2 mM Fluo-5N through the patch pipette. The whole-cell Ca^{2+} current is shown below. The four 90 ms depolarization steps occurred within frames 29, 31, 33 and 35 (100 ms per frame). Scale bar: 5 μm. *B*, the submembranous $[Ca^{2+}]$ averaged over the whole footprint (black) for the same cell shown in *A* was compared with the $[Ca^{2+}]$ of two ROIs (each 10 pixels $\times$ 10 pixels), one ROI centred over a patch of Ca^{2+} channels (green box in *A*) and one remote from Ca^{2+} channels (red box). The black bar indicates the time of the depolarization. Similar results were seen for seven other cells. The cumulative exocytosis events measured by IRM in response to the same stimulus is shown above ($n = 10$ cells).

Discussion

The results of this study demonstrate that the time and place of vesicle fusion in chromaffin cells is not tightly coupled to the opening of Ca^{2+} channels in the surface membrane. Direct visualization of the submembranous Ca^{2+} signal associated with brief openings of Ca^{2+} channels demonstrated that these were

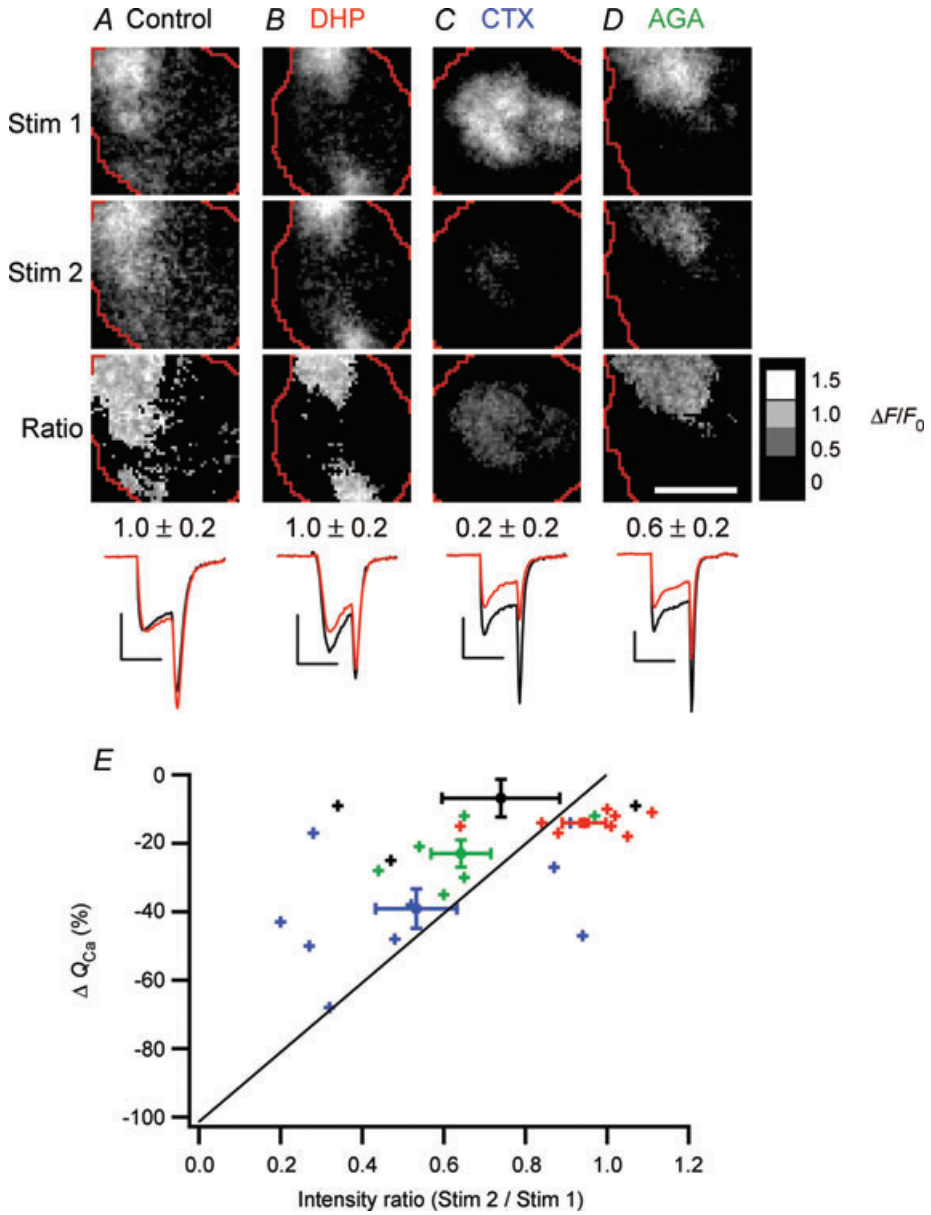

Figure 8. Calcium channel patches in footprints consist primarily of N- and P/Q-type channels
A–D, images of Ca^{2+} influx ($\Delta F/F$) obtained at rest (Stim 1, top row) and in a test condition (Stim 2, second row), as well as the ratio of Stim 2/Stim 1 (Ratio, third row). Each frame is averaged from 6 responses to depolarizations lasting 2 ms. Before and during the second stimulus set (Stim 2), cells were perfused either with normal Ringer solution (*A*), 20 μM nifedipine and 20 μM nimodipine (*B*), 1 μM ω-conotoxin GVIA (*C*) or 200–400 nM ω-agatoxin IVA (*D*). Mean ratio values (± S.D.) over the patch of Ca^{2+} channels are shown below the ratio images. The averaged whole-cell Ca^{2+} currents for Stim 1 (black) and Stim 2 (red) are at bottom; all calibration bars: 200 pA × 2 ms. Scale bar: 5 μm; ratio calibration bar = 1.5 (white), 1.0, 0.5, 0 (black). *E*, collected results ($n = 28$ cells), showing the percentage change in Ca^{2+} influx over the whole cell (ΔQ_{Ca}) *versus* the intensity ratio over the patch of Ca^{2+} channels. Small crosses represent data from individual cells perfused with either control Ringer solution (black), dihydropyridines (red), conotoxin (blue), or agatoxin (green) before collecting the second set of stimulus images. Large markers with error bars represent means. The diagonal line marks the relationship expected if $\Delta F/F$ were directly proportional to Q_{Ca} and all types of Ca^{2+} channels were randomly distributed over the whole surface of the cell, including the footprint.

not discrete microdomains, but large areas, often covering tens of square micrometres (Fig. 4).

Three aspects of the results obtained with Ca^{2+} buffers also argued against tight coupling between sites of granule fusion and Ca^{2+} channels within these large regions of the membrane. First, vesicle fusion in chromaffin cells was very sensitive to EGTA (Fig. 2), a chelator that binds Ca^{2+} ions relatively slowly and which is therefore only effective at reducing the Ca^{2+} signal at micrometre distances from Ca^{2+} channels (Neher, 1998). Second, the rate of vesicle fusion *accelerated* as Ca^{2+} accumulated in the cytoplasm over periods of seconds (Fig. 2*C*). The time scale over which calcium microdomains are generated is three orders of magnitude shorter. Third, BAPTA, a fast chelator of Ca^{2+} ions, was no more effective at slowing the rate of exocytosis than EGTA, which binds Ca^{2+} ions about 60-fold more slowly (Fig. 2*E*). Although the majority of fusion sites were located within areas of the surface membrane containing patches of Ca^{2+} channels, exocytosis also occurred at sites remote from channels (Fig. 6). In addition, asynchronous release after closure of Ca^{2+} channels was an obvious feature of exocytic responses (Fig. 7), providing direct evidence that release did not require Ca^{2+} microdomains generated by closely coupled Ca^{2+} channels. All these observations run counter to the suggestion that fusion of large vesicles in chromaffin cells is driven by localized Ca^{2+} signals similar to those observed at the synapse (Becherer *et al.* 2003; Olivos Ore & Artalejo, 2004).

The results we have presented stand in contrast to those of Becherer *et al.* (2003), who reported that brief (< 100 ms) Ca^{2+} transients could be generated in the footprint of chromaffin cells during 3 s applications of high K^+, localized to submicrometre areas. It is unclear how such localized calcium gradients might be suddenly generated during a maintained depolarization that will lead to widespread diffusion of submembranous Ca^{2+} and channel inactivation (Fig. 7). The approach we have used to detect regions of calcium influx, a depolarization of 2 ms followed by the immediate imaging of the calcium signal over a period of 11 ms, is likely to be a more reliable method for identifying sites of calcium entry, and has been used to detect calcium microdomains at synapses (Tucker & Fettiplace, 1996; Zenisek *et al.* 2003; Beaumont *et al.* 2005). This approach failed to uncover discrete calcium microdomains in chromaffin cells.

Calcium channels distributed over large areas of membrane

On depolarization, calcium influx occurred through areas of the surface membrane covering many tens of squared micrometres, and 'microdomains' could not be detected.

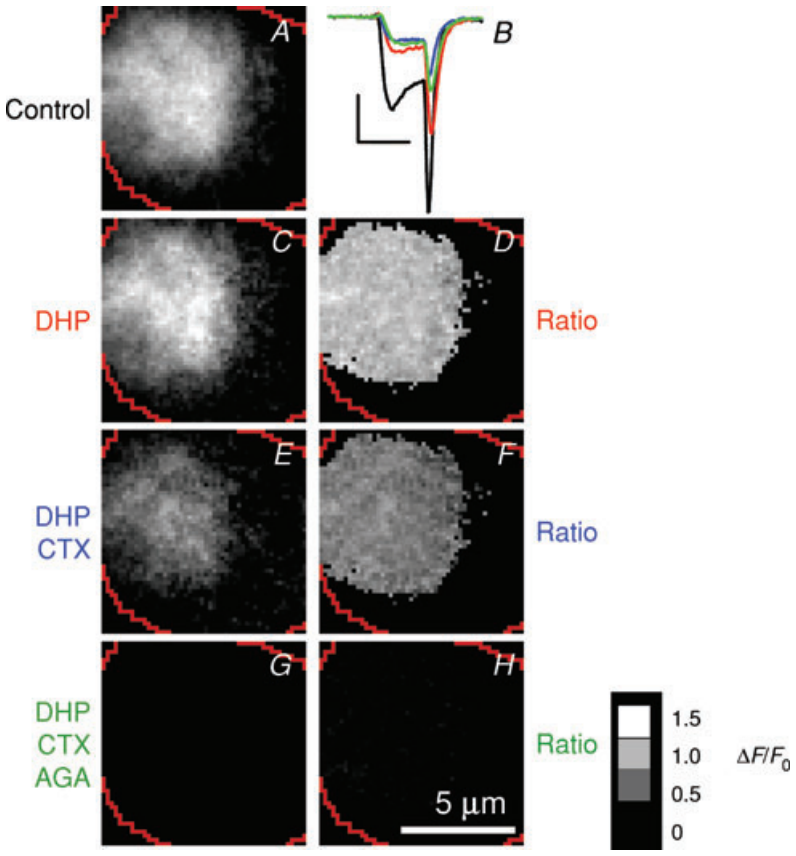

Figure 9. Absence of L-type calcium channels in the footprint
A, images of Ca^{2+} influx ($\Delta F/F$) obtained at rest, then after successively adding 20 μM nifedipine and 20 μM nimodipine (*C*), 1 μM ω-conotoxin GVIA (*E*) and 200–400 nM ω-agatoxin IVA (*G*), all to the same cell. The corresponding ratio images are shown in *D*, *F* and *H*; the Ca^{2+} currents are shown in *B*. Dihydropyridines blocked the majority of Ca^{2+} channels in the surface membrane of this cell as a whole (*B*), but none in the footprint (*D*). Calibration bar in *B*: 200 pA × 2 ms; scale bar, 5 μm; ratio calibration bar = 1.5 (white), 1.0, 0.5, 0 (black).

TIRFM has reliably detected calcium microdomains at the active zones of retinal bipolar cells and hair cells (Zenisek *et al.* 2003; Beaumont *et al.* 2005), so the lack of such signals in chromaffin cells is unlikely to be a limitation of the technique. Although imaging indicated that the density of channels within a patch was not uniform (Figs 6 and 7), it was clear that the Ca^{2+} signal over most areas of the membrane was affected by Ca^{2+} influx over many channels distributed widely.

How many channels formed a patch in a chromaffin cell? The average surface area of a chromaffin cell is about 710 μm^2 (assuming a specific membrane capacitance of 8 fF μm^{-2}), and Ca^{2+} channel patches covered an average of 60% of the footprint in 11 cells. If the estimated 10 000 to 20 000 Ca^{2+} channels (Fenwick *et al.* 1982; Artalejo *et al.* 1992) in a chromaffin cell were distributed homogeneously throughout these patches, the average patch would contain 800–1700 channels at a density of about 25–50 μm^{-2}. These results stand in contrast to the way Ca^{2+} channels are distributed in the membrane of large synaptic terminals, such as ribbon synapses of hair cells, bipolar cells or the calyx of Held, where all channels occur in a few very tight clusters, a fraction of a micrometre in diameter, covering less than 5% of the surface membrane (Roberts *et al.* 1990; Tucker & Fettiplace, 1996; Meinrenken *et al.* 2002; Zenisek *et al.* 2003; Beaumont *et al.* 2005). Electron microscopy and electrophysiology studies in frog hair cells indicate that an average active zone contains about 90 Ca^{2+} channels covering an area of 0.06 μm^2, equivalent to a density of 1500 channels μm^{-2} (Roberts *et al.* 1990). Calcium influx through these tight clusters of channels can be readily observed by imaging (Cohen *et al.* 1991; Tucker & Fettiplace, 1996; Zenisek *et al.* 2003; Beaumont *et al.* 2005).

Excitation–secretion coupling in neuroendocrine cells and synapses

The results of this study allow us to compare the membrane organization of Ca^{2+} channels and fusion sites in chromaffin cells and presynaptic terminals. Synapses provide specific sites of communication between neurons, and release of neurotransmitter occurs at active zones on the spatial scale of hundreds of nanometres directed towards postsynaptic receptors that are similarly localized. In contrast, chromaffin cells in the adrenal gland release catecholamines into the vasculature that travels along the entire apical surface of the cell, and it is across this large region of surface membrane that granules are docked (Chan *et al.* 2005). These distinctive differences in the spatial organization of exocytic sites in neurons and neuroendocrine cells might be correlated with differences in the spatial organization of Ca^{2+} channels. Larger domains of calcium entry in chromaffin cells compared to synapses may reflect the lack of spatial precision in the release of hormones compared to neurotransmitters.

References

Adler EM, Augustine GJ, Duffy SN & Charlton MP (1991). Alien intracellular calcium chelators attenuate neurotransmitter release at the squid giant synapse. *J Neurosci* **11**, 1496–1507.

Albillos A, Neher E & Moser T (2000). R-type Ca^{2+} channels are coupled to the rapid component of secretion in mouse adrenal slice chromaffin cells. *J Neurosci* **20**, 8323–8330.

Ales E, Tabares L, Poyato JM, Valero V, Lindau M & Alvarez de Toledo G (1999). High calcium concentrations shift the mode of exocytosis to the kiss-and-run mechanism. *Nat Cell Biol* **1**, 40–44.

Allersma MW, Bittner MA, Axelrod D & Holz RW (2006). Motion matters: secretory granule motion adjacent to the plasma membrane and exocytosis. *Mol Biol Cell* **17**, 2424–2438.

Almers W (1990). Exocytosis. *Annu Rev Physiol* **52**, 607–624.

Artalejo CR, Adams ME & Fox AP (1994). Three types of Ca^{2+} channel trigger secretion with different efficacies in chromaffin cells. *Nature* **367**, 72–76.

Artalejo CR, Rossie S, Perlman RL & Fox AP (1992). Voltage-dependent phosphorylation may recruit Ca^{2+} current facilitation in chromaffin cells. *Nature* **358**, 63–66.

Beaumont V, Llobet A & Lagnado L (2005). Expansion of calcium microdomains regulates fast exocytosis at a ribbon synapse. *Proc Natl Acad Sci U S A* **102**, 10700–10705.

Becherer U, Moser T, Stuhmer W & Oheim M (2003). Calcium regulates exocytosis at the level of single vesicles. *Nat Neurosci* **6**, 846–853.

Burrone J, Neves G, Gomis A, Cooke A & Lagnado L (2002). Endogenous calcium buffers regulate fast exocytosis in the synaptic terminal of retinal bipolar cells. *Neuron* **33**, 101–112.

Catterall WA (1999). Interactions of presynaptic Ca^{2+} channels and snare proteins in neurotransmitter release. *Ann N Y Acad Sci* **868**, 144–159.

Chan SA, Polo-Parada L & Smith C (2005). Action potential stimulation reveals an increased role for P/Q-calcium channel-dependent exocytosis in mouse adrenal tissue slices. *Arch Biochem Biophys* **435**, 65–73.

Chan SA & Smith C (2001). Physiological stimuli evoke two forms of endocytosis in bovine chromaffin cells. *J Physiol* **537**, 871–885.

Chan SA & Smith C (2003). Low frequency stimulation of mouse adrenal slices reveals a clathrin-independent, protein kinase C-mediated endocytic mechanism. *J Physiol* **553**, 707–717.

Chow RH, Klingauf J, Heinemann C, Zucker RS & Neher E (1996). Mechanisms determining the time course of secretion in neuroendocrine cells. *Neuron* **16**, 369–376.

Chow RH, Klingauf J & Neher E (1994). Time course of Ca^{2+} concentration triggering exocytosis in neuroendocrine cells. *Proc Natl Acad Sci U S A* **91**, 12765–12769.

Cohen MW, Jones OT & Angelides KJ (1991). Distribution of Ca^{2+} channels on frog motor nerve terminals revealed by fluorescent omega-conotoxin. *J Neurosci* **11**, 1032–1039.

Currie KP & Fox AP (1997). Comparison of N- and P/Q-type voltage-gated calcium channel current inhibition. *J Neurosci* **17**, 4570–4579.

Degtyar VE, Allersma MW, Axelrod D & Holz RW (2007). Increased motion and travel, rather than stable docking, characterize the last moments before secretory granule fusion. *Proc Natl Acad Sci U S A* **104**, 15929–15934.

Demuro A & Parker I (2006). Imaging single-channel calcium microdomains. *Cell Calcium* **40**, 413–422.

Engisch KL & Nowycky MC (1996). Calcium dependence of large dense-cored vesicle exocytosis evoked by calcium influx in bovine adrenal chromaffin cells. *J Neurosci* **16**, 1359–1369.

Fenwick EM, Marty A & Neher E (1982). Sodium and calcium channels in bovine chromaffin cells. *J Physiol* **331**, 599–635.

García AG, García-De-Diego AM, Gandía L, Borges R & García-Sancho J (2006). Calcium signalling and exocytosis in adrenal chromaffin cells. *Physiol Rev* **86**, 1093–1131.

Gil A, Viniegra S, Neco P & Gutierrez LM (2001). Co-localization of vesicles and P/Q Ca^{2+}-channels explains the preferential distribution of exocytotic active zones in neurites emitted by bovine chromaffin cells. *Eur J Cell Biol* **80**, 358–365.

Giovannucci DR, Hlubek MD & Stuenkel EL (1999). Mitochondria regulate the Ca^{2+}-exocytosis relationship of bovine adrenal chromaffin cells. *J Neurosci* **19**, 9261–9270.

Herrington J & Bookman RJ (1994). *PULSE CONTROL v4.0: IGOR XOPS for Patch Clamp Data Acquisition and Capacitance Measurements*. University of Miami Press, Miami, FL, USA.

Khimich D, Nouvian R, Pujol R, Tom Dieck S, Egner A, Gundelfinger ED & Moser T (2005). Hair cell synaptic ribbons are essential for synchronous auditory signalling. *Nature* **434**, 889–894.

Kishimoto T, Kimura R, Liu T, Nemoto T, Takahashi N & Kasai H (2006). Vacuolar sequential exocytosis of large dense-core vesicles in adrenal medulla. *EMBO J* **25**, 673–682.

Lara B, Gandía L, Martinez-Sierra R, Torres A & García AG (1998). Q-type Ca^{2+} channels are located closer to secretory sites than L-type channels: functional evidence in chromaffin cells. *Pflugers Arch* **435**, 472–478.

Llobet A, Beaumont V & Lagnado L (2003). Real-time measurement of exocytosis and endocytosis using interference of light. *Neuron* **40**, 1075–1086.

Llobet A, Wu M & Lagnado L (2008). The mouth of a dense-core vesicle opens and closes in a concerted action regulated by calcium and amphiphysin. *J Cell Biol* **182**, 1017–1028.

Long AA, Kim E, Leung HT, Woodruff E 3rd, An L, Doerge RW, Pak WL & Broadie K (2008). Presynaptic calcium channel localization and calcium-dependent synaptic vesicle exocytosis regulated by the Fuseless protein. *J Neurosci* **28**, 3668–3682.

Martin TF (1994). The molecular machinery for fast and slow neurosecretion. *Curr Opin Neurobiol* **4**, 626–632.

Meinrenken CJ, Borst JG & Sakmann B (2002). Calcium secretion coupling at calyx of Held governed by nonuniform channel-vesicle topography. *J Neurosci* **22**, 1648–1667.

Moser T & Neher E (1997). Rapid exocytosis in single chromaffin cells recorded from mouse adrenal slices. *J Neurosci* **17**, 2314–2323.

Naraghi M & Neher E (1997). Linearized buffered Ca^{2+} diffusion in microdomains and its implications for calculation of $[Ca^{2+}]$ at the mouth of a calcium channel. *J Neurosci* **17**, 6961–6973.

Neher E (1998). Vesicle pools and Ca^{2+} microdomains: new tools for understanding their roles in neurotransmitter release. *Neuron* **20**, 389–399.

Neher E (2006). A comparison between exocytic control mechanisms in adrenal chromaffin cells and a glutamatergic synapse. *Pflugers Arch* **453**, 261–268.

Neher E & Sakaba T (2008). Multiple roles of calcium ions in the regulation of neurotransmitter release. *Neuron* **59**, 861–872.

Nofal S, Becherer U, Hof D, Matti U & Rettig J (2007). Primed vesicles can be distinguished from docked vesicles by analyzing their mobility. *J Neurosci* **27**, 1386–1395.

Olivos Ore L & Artalejo AR (2004). Intracellular Ca^{2+} microdomain-triggered exocytosis in neuroendocrine cells. *Trends Neurosci* **27**, 113–115.

Perrais D, Kleppe I, Taraska J & Almers W (2004). Recapture after exocytosis causes differential retention of protein in granules of bovine chromaffin cells. *J Physiol* **560**, 413–428.

Rickman C, Meunier FA, Binz T & Davletov B (2004). High affinity interaction of syntaxin and SNAP-25 on the plasma membrane is abolished by botulinum toxin E. *J Biol Chem* **279**, 644–651.

Roberts WM, Jacobs RA & Hudspeth AJ (1990). Colocalization of ion channels involved in frequency selectivity and synaptic transmission at presynaptic active zones of hair cells. *J Neurosci* **10**, 3664–3684.

Robinson IM, Finnegan JM, Monck JR, Wightman RM & Fernandez JM (1995). Colocalization of calcium entry and exocytotic release sites in adrenal chromaffin cells. *Proc Natl Acad Sci U S A* **92**, 2474–2478.

Robitaille R, Adler EM & Charlton MP (1990). Strategic location of calcium channels at transmitter release sites of frog neuromuscular synapses. *Neuron* **5**, 773–779.

Schoch S & Gundelfinger ED (2006). Molecular organization of the presynaptic active zone. *Cell Tissue Res* **326**, 379–391.

Serulle Y, Sugimori M & Llinás RR (2007). Imaging synaptosomal calcium concentration microdomains and vesicle fusion by using total internal reflection fluorescent microscopy. *Proc Natl Acad Sci U S A* **104**, 1697–1702.

Seward EP & Nowycky MC (1996). Kinetics of stimulus-coupled secretion in dialyzed bovine chromaffin cells in response to trains of depolarizing pulses. *J Neurosci* **16**, 553–562.

Sun JY, Wu XS, Wu W, Jin SX, Dondzillo A & Wu LG (2004). Capacitance measurements at the calyx of Held in the medial nucleus of the trapezoid body. *J Neurosci Methods* **134**, 121–131.

Tucker TR & Fettiplace R (1996). Monitoring calcium in turtle hair cells with a calcium activated potassium channel. *J Physiol* **494**, 613–626.

Xu T, Binz T, Niemann H & Neher E (1998). Multiple kinetic components of exocytosis distinguished by neurotoxin sensitivity. *Nat Neurosci* **1**, 192–200.

Zenisek D, Davila V, Wan L & Almers W (2003). Imaging calcium entry sites and ribbon structures in two presynaptic cells. *J Neurosci* **23**, 2538–2548.

Zhou Z & Misler S (1995). Action potential-induced quantal secretion of catecholamines from rat adrenal chromaffin cells. *J Biol Chem* **270**, 3498–3505.

Author contributions

All authors contributed to the conception, analysis and interpretation of experiments as well as writing and revising the article.

Authors' present addresses

M. M. Wu: Department of Molecular and Cellular Physiology, Stanford University School of Medicine, Stanford, CA 94305, USA.

A. Llobet: Laboratori de Neurobiologia-CIBERNED, IDIBELL-Universitat de Barcelona 08907, L'Hospitalet de Llobregat, Spain.